



HAL
open science

Stabilization and Dynamics of Pure Hydrogen Swirling Flames Using Cross-Flow Injection

Nicolas Vaysse, Daniel Durox, Ronan Vicquelin, Sébastien Candel, Antoine Renaud

► **To cite this version:**

Nicolas Vaysse, Daniel Durox, Ronan Vicquelin, Sébastien Candel, Antoine Renaud. Stabilization and Dynamics of Pure Hydrogen Swirling Flames Using Cross-Flow Injection. ASME Turbo Expo 2023: Turbomachinery Technical Conference and Exposition, Jun 2023, Boston (MA), United States. 10.1115/GT2023-101977 . hal-04564363

HAL Id: hal-04564363

<https://hal.science/hal-04564363v1>

Submitted on 30 Apr 2024

HAL is a multi-disciplinary open access archive for the deposit and dissemination of scientific research documents, whether they are published or not. The documents may come from teaching and research institutions in France or abroad, or from public or private research centers.

L'archive ouverte pluridisciplinaire **HAL**, est destinée au dépôt et à la diffusion de documents scientifiques de niveau recherche, publiés ou non, émanant des établissements d'enseignement et de recherche français ou étrangers, des laboratoires publics ou privés.



Distributed under a Creative Commons Attribution 4.0 International License

GT2023-101977

STABILIZATION AND DYNAMICS OF PURE HYDROGEN SWIRLING FLAMES USING CROSS-FLOW INJECTION

Nicolas Vaysse^{1*}, Daniel Durox¹, Ronan Vicquelin¹, Sébastien Candel¹, Antoine Renaud¹

¹Laboratoire EM2C, CNRS, CentraleSupélec, Université Paris-Saclay, 3, rue Joliot Curie, 91192 Gif-sur-Yvette cedex, France
Email: nicolas.vaysse@centralesupelec.fr

ABSTRACT

Hydrogen combustion is currently being considered as a possible means of decarbonization of power generation and air transportation. However, hydrogen raises difficult issues including that of NOx emissions linked to the high flame temperature and that of flashback caused by its high burning velocity. Innovative injection schemes are required allowing operation under lean conditions by enhancing mixing to avoid hotspots. In addition, the flame needs to be stabilized at a distance from solid boundaries to reduce thermal loads and should offer a low sensitivity to disturbances and instability. These issues are investigated with systematic experiments carried out in a single injector laboratory-scale combustor operating at atmospheric pressure, a configuration that was already used to examine the dynamics of spray flames. The atomizer is replaced by a special unit (CFI-X) that allows gaseous hydrogen injection in crossflow and mixing with the air stream set in rotation by a radial swirler. The flame behavior formed by this device is examined as a function of thermal power and global equivalence ratio. The injection head recess is also varied to change the level of mixing in the system and see how it influences thermo-acoustic instabilities. Flame structures visualized through OH* light emission images are used to classify the various flame patterns and distinguish domains where the flame is detached from the injector outlet. Variations of the injection head recess with respect to the outlet, swirl number and chamber length provide a comprehensive view of the operating regimes. It is found that the flames remain attached to the injector at low power and that detached flames are obtained in

the high-power range. Dynamical phenomena leading to oscillations coupled by longitudinal chamber modes are observed in an intermediate thermal power range. The corresponding data are interpreted with a stability analysis that defines instability bands for the product of a time delay by the frequency of oscillation. It is found that unstable flames belong to the first of these bands. It is also observed that detached flames that are the most interesting in terms of thermal loads and mixing may also belong to the band of instability but do not give rise to oscillations and are therefore less sensitive to instability.

Keywords: Hydrogen combustion, Stabilization, Swirling flames, Combustion dynamics.

NOMENCLATURE

\mathcal{P}_{th}	Theoretical thermal power [kW]
ϕ	Global equivalence ratio
s	Mass stoichiometric coefficient
P	Ambient pressure [Pa]
T	Ambient temperature [K]
q	Volumetric flow rate [$\text{m}^3 \cdot \text{s}^{-1}$]
\dot{m}	Mass flow rate [$\text{kg} \cdot \text{s}^{-1}$]
ρ	Density [$\text{kg} \cdot \text{m}^{-3}$]
W	Molar mass [$\text{kg} \cdot \text{mol}^{-1}$]
a	Subscript for air flow
H_2	Subscript for hydrogen flow
d_e	Injector outlet diameter [mm]
h_r	Recess length [mm]
l_c	Quartz tube length [mm]

*Address all correspondence to this author.

S	Conventional swirl number
σ	Pressure drop coefficient
J	Hydrogen to air momentum flux ratio
HF	Axial position of flame foot [mm]
RF	Radial position of flame foot [mm]
HG	Flame height: flame barycenter axial position [mm]
α	Aperture angle of the flame [°]
ζ	Specific impedance
\mathcal{F}	Flame transfer function
φ_ζ	Phase of the impedance [rad]
φ_F	Phase of the flame transfer function [rad]
ω_{1i}	Linear growth rate [rad. s ⁻¹]

1 INTRODUCTION

Hydrogen is now considered as a possible means for the decarbonization of industrial processes, energy production and air transportation. It offers a high specific heating value and carbon-free combustion that makes it a credible alternative to current fuels. However, its physical and reactive characteristics differ from those of standard aviation fuels and they raise new risks [1, 2]. The large burning velocity of hydrogen in air makes it prone to flashback and its high flame temperature may potentially enhance the NOx emissions induced by the Zeldovich thermal oxidation mechanisms [3]. Many issues need to be tackled if one wishes to replace the standard liquid or gaseous fuels with hydrogen. In terms of combustion, one central issue is to devise a scheme that will allow flame stabilization away from solid boundaries, including injector, chamber backplane and side walls. A second issue is to make sure that the flame established in the burner will be sufficiently well mixed and lean to eliminate regions of nearly stoichiometric conditions, reduce burning temperatures and limit NOx emissions. A third issue concerns the dynamical behavior of the system and the definition of flame configurations that avoid bistable regimes of operation and that are less sensitive to perturbations and less prone to transients like flashback and combustion instabilities coupled by acoustic modes.

Targeting these objectives, several injection geometries have been investigated more recently to enhance mixing while controlling flashback. In premixed configurations, axial air injection at high speed [4–6] in combination with swirl [7] have been shown as possible ways to increase the resistance to flashback. While axial air injection helps to lower the flashback limit of premixed hydrogen flames [5] while ensuring a sufficient mixing that maintains low NOx emissions [4, 6], swirling flows enable to reduce wall boundary layer-induced flashback (WBLF) below $\phi \approx 0.75$ for premixed hydrogen-air flames [7]. In non-premixed hydrogen-air flames, swirl number and momentum flux ratio determine flame stabilization and NOx emissions [8,9]. It is shown that for double swirl configurations, increasing the power and the internal swirl number allows the stabilization of lifted flames,

whereas a low momentum flux ratio favors the flame reattachment to the nozzle. The flame stabilization can be obtained using injectors equipped with a central bluff body. This method allows flame anchoring of premixed methane flames enriched with hydrogen [10]. Empirical models of turbulent flame speed have been developed to help avoid flashback risks with bluff body-stabilized hydrogen and methane flames [11]. It is found that increasing the hydrogen content in the CH₄/H₂ blend leads to a change of flame shape yielding stable anchored flames, which become unstable when the hydrogen volume fraction exceeds a certain threshold [10]. The use of bluff body stabilization is probably not technically feasible because of the high thermal loads induced by the flame on the stabilizer.

The central idea of the present investigation is to combine swirl with transverse injection of hydrogen to enhance mixing and anchor the flame at a distance from the injection unit. Such a system has been used for oxy-colorless distributed combustion applied to mixtures of methane with hydrogen [12]. This aerodynamic stabilization scheme resulting from radial swirlers is targeted at reducing thermal loads induced by the flame on the chamber backplane and injection system. The radial injection of hydrogen in a strong helicoidal air flow is aimed at augmenting mixing to form a nearly homogeneous mixture ratio distribution that will be sufficiently lean to avoid NOx formation. This late stage premixing is meant to lower the risks of flashback, as it has been observed on micro-mix combustors, featuring a multiplicity of crossflow hydrogen injection units [13]. The influence of thermal power and global equivalence ratio is here systematically explored to sort out the various flame structures and identify operating conditions leading to stabilization at a distance from the injection unit giving rise to lifted flames.

Effects of geometrical parameters such as the chamber length and the recess of the injection head are also considered. The chamber length is used to change the frequency of the resonant modes of the system and thus may serve to trigger thermo-acoustic instabilities. Increasing the injection head recess enhances mixing inside the injector but this may also promote instabilities. It is known for example that the recess in rocket engines coaxial injectors enhances hydrodynamic instabilities of the coaxial streams of propellants augmenting the flame expansion rate [14]. For gaseous fuels, theoretical models confirm the effect of injection recess length [15] while some recent investigations on hydrogen-enriched premixed CH₄/air flames indicate that longer chamber sizes give rise to self-sustained thermo-acoustic oscillations [16]. Experiments in our group on swirled spray flames [17] confirm that the atomizer recess notably influences the dynamical behavior of the combustion system.

This article begins with a brief presentation of the experimental facility and injection unit designated in what follows as CFI-X (section 2). The different stable flame shapes obtained with

this burner are presented in section 3, along with the geometrical analysis used for their classification. The dynamical behavior observed under certain operating conditions is investigated in section 4 using combined optical imaging and acoustic measurements. Finally, the influence of recess and chamber length is investigated in section 5. Experimental data are shown to comply with a theoretical instability model defining regions of instability using time-lag concepts.

2 EXPERIMENTAL SETUP

The experimental system is derived from the SICCA-Spray set up [18], previously used to study swirled premixed and spray hydrocarbon flames. This configuration was equipped with a hollow cone spray atomizer, which is here replaced by a crossflow injection head with identical external dimensions (Fig. 1(c)). The injector is designated in what follows as Cross Flow Injector - exp (CFI-X). This unit enables gaseous hydrogen injection in the swirled air flow through six radial ports of diameter $d_i = 1.5$ mm. The mass flow rates of air and hydrogen are controlled by two *Bronkhorst* EL-FLOW meters with full-scale capacities of 150 NL/min for air and 30 NL/min for hydrogen and with a relative accuracy of 0.5%. In this work, the thermal power and global equivalence ratio are deduced from the mass flow rates using:

$$\mathcal{P}_{th} = \Delta h^0 \dot{m}_{H_2} \quad (1)$$

$$\phi = s \dot{m}_{H_2} / \dot{m}_a \quad (2)$$

where the lower heating value of hydrogen is $\Delta h^0 = \text{LHV} = 119.9 \text{ MJ kg}^{-1}$ and the mass stoichiometric coefficient $s = 34.32$ is based on air and hydrogen. One key parameter that is widely used to control jets in cross-flow is the hydrogen/air momentum flux ratio calculated in the vicinity of the injection ports [19]:

$$J = \frac{\rho_{H_2} v_{H_2}^2}{\rho_a v_a^2} = \kappa \phi^2 \quad (3)$$

This ratio may be linked to the square of the equivalence ratio with a proportionality constant κ that is a function of s , ρ_{H_2}/ρ_a and of geometrical characteristics of the CFI-X unit. The bulk velocities v_{H_2} and v_a are respectively those of the hydrogen jet and the air flow in the injection section. In this work, the values of thermal power and equivalence ratio respectively belong to the following ranges $\mathcal{P}_{th} \in [0.9; 5.3] \text{ kW}$ and $\phi \in [0.2; 0.6]$, resulting in J values ranging from 0.03 to 0.31. In the baseline configuration the injection head is located at a distance $h_r = 6.75$ mm from the injector outlet. This recess can be varied between 2.75 mm and 9.75 mm to study its influence on flame stabilization [17]. Simple 2D trajectory models show that hydrogen flow penetrates inside the airflow and is not impinging the injector wall. Mixing

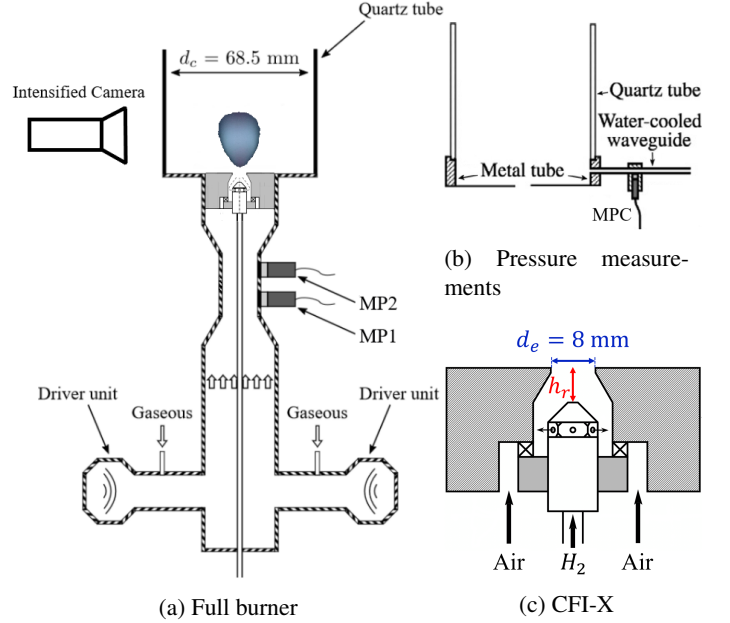


FIGURE 1: Experimental setup, adapted from [18]: full burner for (a) flame visualization, (b) pressure measurements, and (c) CFI-X with atomizer replaced by the crossflow injection head.

is here governed by the momentum flux ratio and by the presence of a tangential flow velocity inside and outside the injection unit.

The plenum (Fig. 1(a)) comprises a cylindrical channel connected on its lower side to a couple of driver units and on its upper side to the injection block comprising the injection unit. The injector outlet has a diameter $d_e = 8$ mm. The central channel has a constant section and comprises slots for microphones. Pressure signals are collected with three *Brüel & Kjaer* type 4938 microphones, mounted with type 2670 preamplifiers, with a relative precision of 1%. Two of them are located in the plenum, and the third one measures the pressure at the base of the chamber through a water-cooled waveguide mounted on an annular metal piece directly placed on the backplane (Fig. 1(b)). The metallic annular piece has a diameter equal to that of the chamber $d_c = 68.5$ mm and is $l_m = 15$ mm high.

The combustion chamber is constituted by a quartz tube with an internal diameter of $d_c = 68.5$ mm. Several tubes of constant diameter are used, with lengths l_q ranging from 100 mm to 450 mm. The chamber length for the baseline geometry is $l_c = l_q = 150$ mm. For flame visualization, the chamber microphone is not mounted so these are the total chamber lengths, but the pressure measurements are performed with 15 mm longer chamber sizes.

The air flow passes through a tangential swirler designated as 707 with six holes of diameter $d_{sc} = 3.5$ mm and deviation with respect to the radial direction $R_0 = 5.5$ mm. The swirl intensity is indicated in this work using the conventional number as defined in [20]:

$$S = \int_0^{R_{lim}} \rho \overline{U_\theta} \overline{U_x} r^2 dr / [R \int_0^{R_{lim}} \rho \overline{U_x}^2 r dr] \quad (4)$$

where $\overline{U_x}$ and $\overline{U_\theta}$ are respectively the mean axial and tangential components of the velocity field in the near vicinity of the injector outlet, R is the injector outlet radius and R_{lim} an integration radius that is here taken equal to $2R$. Due to geometrical constraints in the Laser Doppler Anemometry (LDA) measurement of the axial velocity, the swirl number is determined at 2.5 mm above the chamber backplane. With the 707 swirler, the measured swirl number is $S = 0.60$ and the pressure loss coefficient is $\sigma = \Delta p / [(1/2)\rho U_b^2] = 3.25$ [21], where U_b designates the axial bulk velocity at the injector outlet. Another swirler, designated as 726 with a pressure loss coefficient of $\sigma = 5.37$ and swirl number $S = 0.74$, is also used to see how this parameter influences the flame configuration.

Flame images are obtained using a *Princeton Instruments* PI-MAX4 intensified camera. An Asahi Spectra XBPA310 optical bandpass filter centered on 310 nm is used to record OH^* chemiluminescence emission from the flame. Another camera covering the visible spectrum is employed to capture natural light emission. The corresponding images provide information about the burnt gas location, water vapor and the blue emission being suspected to correspond to reaction products, either excited water molecules or hydrogen peroxide [22]. OH^* images are processed using an Abel deconvolution and their contour is determined with the Otsu thresholding method. The mean images that are shown in this work are formed by accumulating 30 frames, each of them recorded with a gate width of $500 \mu\text{s}$. The instantaneous images that are used to study the flame dynamics are recorded with a gate width of $100 \mu\text{s}$ by sets of 30 images. Phase-averaged OH^* images used to capture cyclic dynamical phenomena are obtained by triggering the camera with the rising zero crossing of the band-pass filtered MP2 plenum microphone signal. The different gate delays are deduced from the signal frequency determined in real-time to obtain 12 phase images during the cycle.

3 STABILIZATION MECHANISMS

It is natural to examine flame structures revealed by images of visible light and OH^* chemiluminescence in the UV range. The visible light is faint but may be recorded by making use of a long exposure consumer-grade camera. Typical results are displayed in Fig. 2. The natural light image (Fig. 2(a)) features a pale blue emission region that corresponds to the intersection of the blue radiation from the hydrogen flame and the optical range of the

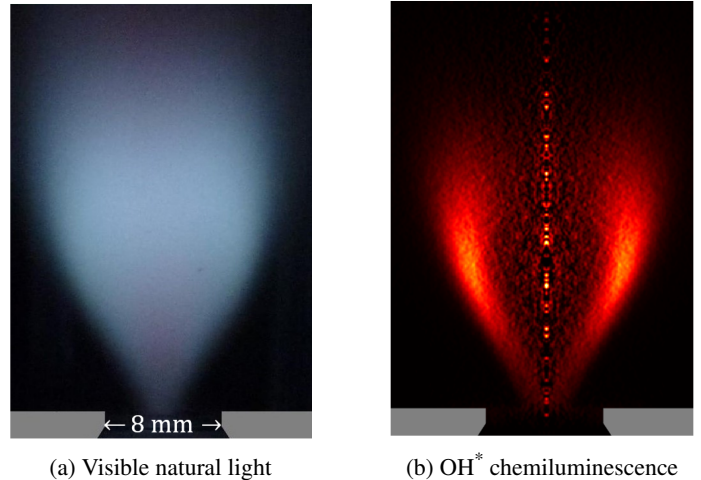


FIGURE 2: Hydrogen/air flames obtained with the SICCA-H2 setup at thermal power $\mathcal{P}_{th} = 4.6$ kW and global equivalence ratio $\phi = 0.42$, in (a) visible light emission, line of sight integrated, and (b) OH^* chemiluminescence after Abel deconvolution. The swirl number is $S = 0.60$ (swirler 707), the chamber length is $l_c = 150$ mm and the injection head recess is $h_r = 6.75$ mm.

camera, which roughly covers the visible range and the near-UV and near-infrared regions. One also distinguishes at the top and at the foot of the flame a very slight emission in the red that originates from hot water vapor molecules.

A different view of the flame is provided by the Abel transformed OH^* chemiluminescence displayed in Fig. 2(b). The excited hydroxyl radical is essentially present in the reaction layer where chemical conversion takes place. In this image, the flame is detached from the injector outlet and the maximum emission intensity is around 12 mm above the backplane. The level of OH^* radiation originating from the inner core is low indicating that this region is occupied by recirculating combustion products that anchor the flame. It is interesting to note that the OH^* Abel transformed images notably differ from the visible light emission images and that they provide a better indication on the mean position and shape of the chemical conversion region in the flame.

Stable flame shapes and structures

It makes sense to use OH^* Abel transformed images to sort out the various flame configurations and regimes of operation. This is here accomplished for a fixed injector geometry by varying the flow rates of hydrogen and air. This allows distinguishing three different stable flame shapes: attached “V” flames, and two types of detached or lifted flames (Figs. 3(a), 3(b) and 3(c)). Starting from the lifted flame in Fig. 3(b), reducing the power leads to an attached “V”-flame where the flame is anchored or close to the injection system tip. Increasing the power at constant ϕ leads to

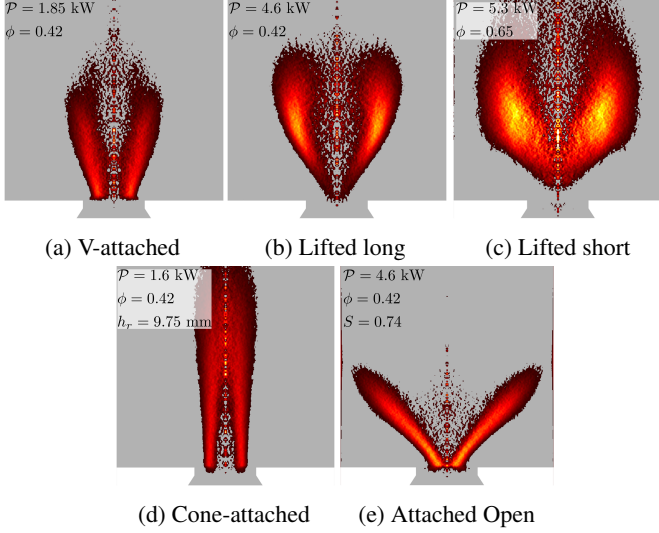


FIGURE 3: Abel-deconvoluted OH^* chemiluminescence images of different flame shapes observed with the tube length $l_c = 150$ mm. The swirl number is (a,b,c,d) $S = 0.60$ and (e) $S = 0.74$. The recess length is (a,b,c,e) $h_r = 6.75$ mm and (d) $h_r = 9.75$ mm. The global equivalence ratio is (a,b,d,e) $\phi = 0.42$ and (c) $\phi = 0.65$. The thermal power is (a) $\mathcal{P}_{th} = 1.85$ kW, (b,e) $\mathcal{P}_{th} = 4.6$ kW, (c) $\mathcal{P}_{th} = 5.3$ kW and (d) $\mathcal{P}_{th} = 1.6$ kW.

lifted flames (from Figs. 3 (a) to (b)). A further increase in \mathcal{P}_{th} or ϕ yields a shorter flame with a thicker and broader brush as in Fig. 3(c). The flame has a lower aspect ratio between front width and height and is thus designated as "lifted short". At low thermal power, increasing the recess length keeps the flame anchored but induces a new configuration characterized by a longer vertical extension and a flame merging at a distance of a few diameters above the injector outlet to form a conical flame (Fig. 3(d)). Using the same operating conditions as for the lifted-long flame (Fig. 3(b)) and increasing the swirl number from 0.60 to 0.74 leads to an attached wide open flame (Fig. 3(e)). This fifth stabilization mode features thinner regions with strong OH^* signal than those found for the V-attached flames. Thus, when the swirl number is increased above a certain level, the flame tends to attach to the injector and expand sideways, indicating that the central recirculation zone has become more intense. From this observation one infers that the swirl number should not exceed a certain limit to obtain regimes of combustion where the flame is detached from the injection unit.

Operating conditions for lifted flames

To determine the operating conditions where the flame is detached, it is convenient to characterize the flame geometry with four indices:

1. The height of the flame foot above the burner (HF) detected using the Otsu thresholding method to determine the lowest point of the contour,
2. The height of flame barycenter height (HG), based on OH^* intensity integrated over the flame perimeter,
3. The radial position of the flame foot (RF),
4. The angle (α) between the flame front line (from foot to top of one half of the Abel-inverted image) and the burner axis.

Figure 4 shows the evolution of these four metrics as functions of \mathcal{P}_{th} and ϕ for the baseline geometry. Note that the swirl number $S = 0.60$ is fixed by the swirler geometry but its value may perhaps slightly change when the hydrogen flow rate is varied. In these experiments the fresh stream bulk velocities at the injector outlet range from 20.5 m s^{-1} to 60.9 m s^{-1} . The first two metrics may serve to distinguish attached and detached flame structures. The lifted flames dominate at high power, and an increase in the global equivalence ratio leads to shorter and thicker flame fronts. At a fixed equivalence ratio, the flame is attached to the injector at low thermal power and detaches from the injector beyond a critical power of $\mathcal{P}_{th, \text{lift}} \approx 3$ kW. Above 4 kW, the flame foot position becomes nearly independent of the power. It is also found that HF/d_e and HG/d_e increase with the equivalence ratio. This trend prevails in an intermediate power range up to 5 kW, where a change of flame shape is observed. Beyond that value, the flames are anchored at a lower distance of the injector and the flame front opens up, as shown in Fig. 4. This is accompanied by a notable change in the flame angle α . The foot is closer to the burner axis, resulting in a flatter flame. This behavior is more pronounced when the global equivalence ratio is augmented. Apart from zero foot height, these V-attached flames are characterized by a low barycenter height. Additionally, at constant power and increasing equivalence ratio, the detached flames foot height (HF) and their height above burner (HG) increase in a similar fashion. This suggests that the vertical size of the flame deduced from the OH^* average intensity images remains roughly constant for all shapes.

It is next instructive to gather all the tested operating conditions in a stability map (Fig. 5) that shows the intervals where the flames remain lifted and those where they are attached to the injector unit. Lifted flames prevail in the high power range $\mathcal{P}_{th} > 3$ kW and for equivalence ratios above $\phi \approx 0.42$. This conclusion should however be taken with caution because of the lack of data pertaining to high power and leaner conditions. Because of mass flow meter limitations, data are also missing for low power-richer flames. For high-power flames, increasing the equivalence ratio leads to a thicker flame front in addition to a probably better premixing of the hydrogen in the air flow due to the accompanying increase of the momentum flux ratio J for the jet-in-crossflow fuel injection. The average flame temperature might rise but the presence of hot spots would be better controlled. This could be

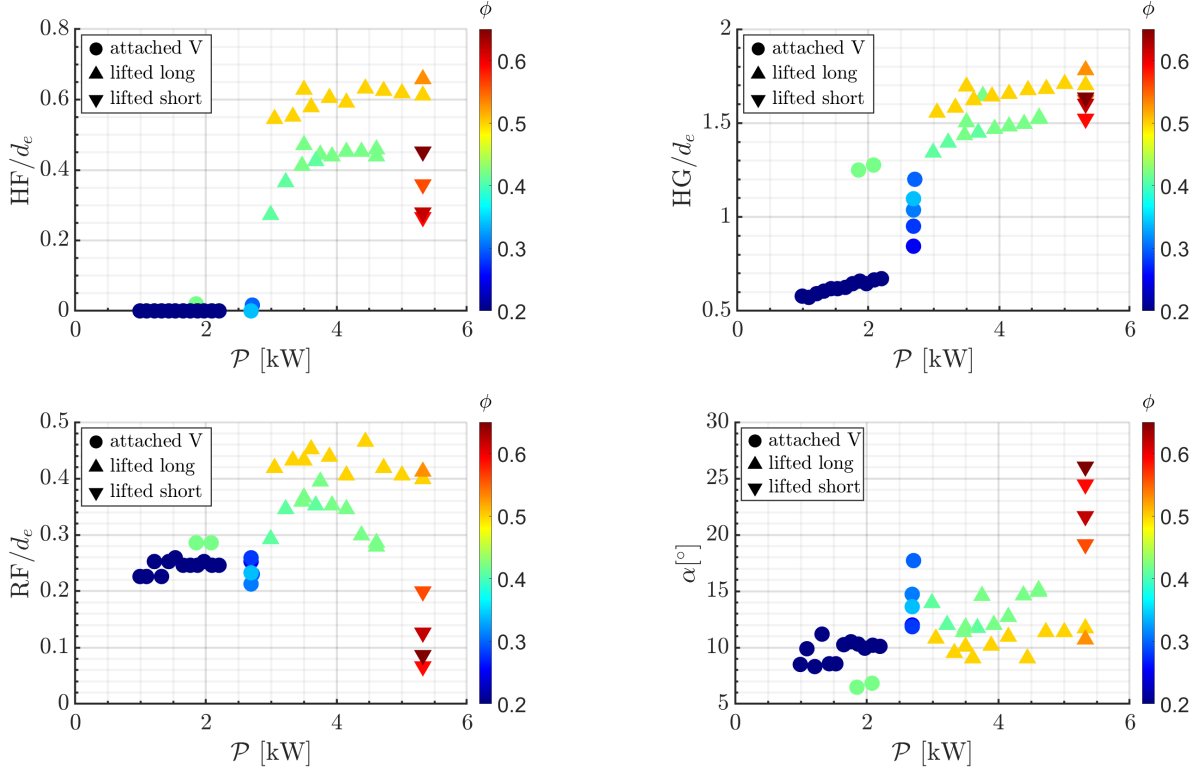


FIGURE 4: Evolution of the four metrics HF (foot height), HG (height of the barycenter), RF (foot radial position) and α (opening angle) as a function of thermal power \mathcal{P}_{th} and global equivalence ratio ϕ , for all the operating points used with baseline geometry parameters: $S = 0.60$, $h_r = 6.75$ mm and $l_c = 150$ mm.

a possible way to maintain high power and low emissions while still stabilizing the flame at a distance from the combustor walls. However, if one intends to increase J at a constant equivalence ratio, it is necessary to modify the geometry, for example by reducing the diameter d_i of the hydrogen outlets.

The risk of flashback leading to attached flames prevails at low power. In this range one also observes unstable configurations that are marked by the black squares in the \mathcal{P}_{th}, ϕ operating map displayed in Fig. 5. Flame unsteadiness is found in the intermediate power range and for intermediate global equivalence ratios. This unstable domain is further investigated in section 4.

Effect of recess on flame stabilization

Changing the injection head location inside the injector leads to different flame configurations for the same operating point as can be seen in Fig. 6. The variations in recess result in flame structure modifications with respect to the flame geometry appearing in Fig. 3. The lifted flame (operating conditions 4) remains detached regardless of the recess length. For certain operating conditions one also observes dynamical changes. This is the case for the cone-attached flame at $h_r = 9.75$ mm (point 2) which becomes unstable for a low recess value, passing by an

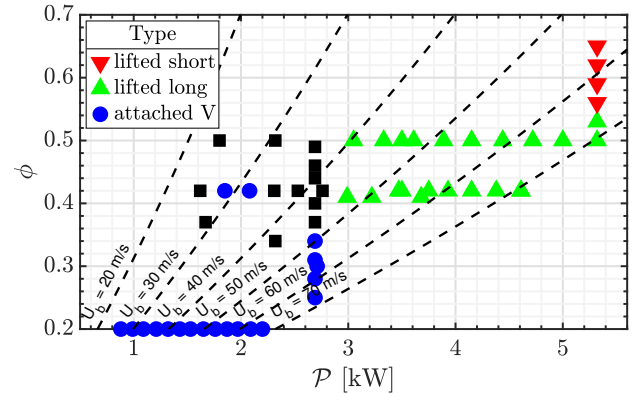


FIGURE 5: Types of flame shapes obtained with the baseline geometry: $S = 0.60$, $h_r = 6.75$ mm and $l_c = 150$ mm, as a function of thermal power \mathcal{P}_{th} and global equivalence ratio ϕ . The black squares correspond to unstable points for this geometry. Dashed lines represent iso-bulk velocities of the fresh gases.

unsteady flapping state on the verge of lean blow out at $h_r = 6.75$ mm. Such an unsteady flapping state can also be observed at low

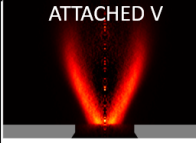
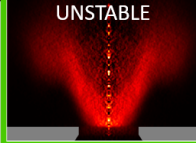
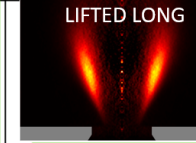
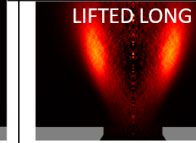
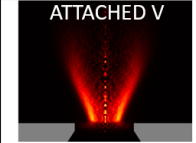
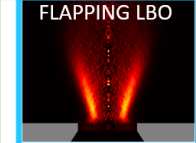
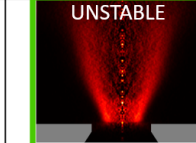
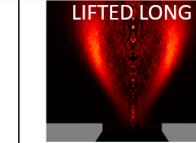
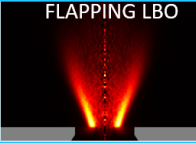
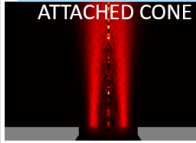
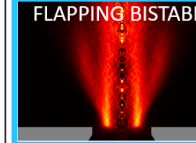
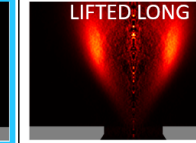
Operating Conditions	(2.2 kW ; 0.20) → $J = 0.03$	(1.62 kW ; 0.42) → $J = 0.13$	(2.31 kW ; 0.42) → $J = 0.13$	(4.61 kW ; 0.42) → $J = 0.13$
h_r \ Point	1	2	3	4
2.75 mm	ATTACHED V 	UNSTABLE 	LIFTED LONG 	LIFTED LONG 
6.75 mm	ATTACHED V 	FLAPPING LBO 	UNSTABLE 	LIFTED LONG 
9.75 mm	FLAPPING LBO 	ATTACHED CONE 	FLAPPING BISTABLE 	LIFTED LONG 

FIGURE 6: Abel transformed OH^* images showing the recess length influence on the flame pattern at four operating points. The chamber length is $l_c = 150$ mm and the swirl number $S = 0.60$. Points 2 and 4 respectively correspond to the conical flame (Fig. 3(d)) and to the lifted flame (Fig. 3(b)). Blue-framed images indicate flapping while green-framed images correspond to thermoacoustic instabilities.

equivalence ratio with a long recess (point 1).

Finally, a thermoacoustically unstable flame is observed at a medium recess value (point 3) which can be stabilized either as a lifted flame when the injection head is close to the chamber backplane, or as an unsteady bistable flame when the recess takes large values. The latter behavior is further described in Fig. 8. For all these operating points 2, 3 and 4, the momentum flux ratio ($J=0.13$) remains independent of the recess as it is a local quantity computed with a constant air velocity magnitude along the mixing zone. However, the level of mixing might be changed by the recess h_r due to the influence of the turbulent swirled air flow. For example, although J remains constant, the lowest injector position might lead to better premixing due to turbulence acting along a higher mixing length. This could explain the presence of the conical shape both at points 2 and 3.

4 FLAME DYNAMICS

At this stage it is natural to examine the dynamical characteristics of the flames formed by the CFI-X injector and more specifically consider cases where thermoacoustic instabilities are manifested. One may generally observe that there are few studies devoted to the thermoacoustic instabilities of hydrogen-air flames that could be used in aero-engine applications, the existing work being focused on methane-hydrogen blends [10, 16]. We first consider a case where the flame is unconditionally stable independently of the chamber length, a situation in which the flame appears to be insensitive to disturbances and does not give rise to oscillations

whatever the frequency of the mode that might couple combustion with the acoustics of the system. We then examine a case where the flame is flapping between two patterns. The final subsection is devoted to a self-sustained oscillation that is typical of thermoacoustic coupling.

An unconditionally stable flame

It is indicated in the previous section that when the swirl number is increased from $S = 0.60$ to $S = 0.74$ detached flames shown in Fig. 3(b) reattach to the injector and rapidly expand in the lateral direction (Fig. 3(e)). The corresponding pattern features flame branches that are thinner than those observed for the V-attached flames. The flame angle of $\alpha = 31.4^\circ$ is higher than that of lifted short flames (Fig. 4). The most intriguing characteristic of this kind of strong swirling flame is its unconditional stability whatever the chamber length. Changes in this length which change the frequency of the corresponding acoustic mode do not give rise to unstable oscillations. Figure 7 shows the contours of 30 line-of-sight integrated flame images, recorded with a reduced gate width of $100 \mu\text{s}$ to capture the instantaneous behavior of the flame. This is accomplished by first classifying the images in two groups and applying the Otsu method in combination with a method that filters out points that do not belong to the flame front. The resulting set of contours (Fig. 7) indicates that the location of the flame front does not change over time, emphasizing the strong stability of this open attached flame.

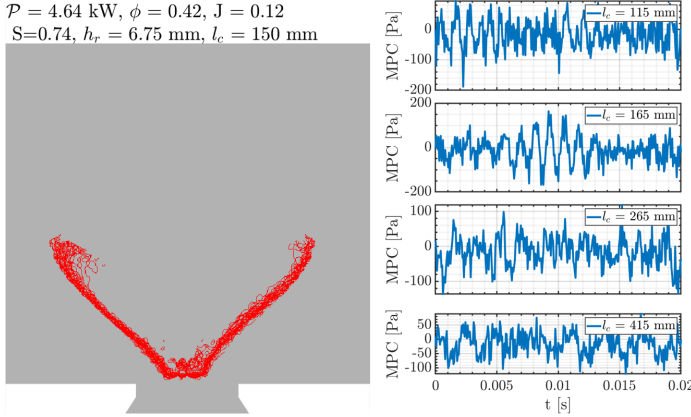


FIGURE 7: Left: contours of 30 line of sight integrated OH^* intensity images, belonging to the domain where the chemical reaction takes place. These contours delineate flame fronts. The operating point is $\mathcal{P}_{th} = 4.61 \text{ kW}$ and $\phi = 0.42$, with $S = 0.74$, $h_r = 6.75 \text{ mm}$ and $l_c = 150 \text{ mm}$. Right: Time evolution of pressure at the chamber backplane. The pressure is measured for the same operating point, recess length h_r and swirler type, but for different chamber lengths, ranging from 115 to 415 mm.

The power spectrum of the pressure signal at the chamber backplane expressed as the sound pressure level in each frequency band $\text{SPL}_{\Delta f}$ remains below 100 dB. In contrast the $\text{SPL}_{\Delta f}$ of unstable flames that are described in what follows may reach 130 dB. Fluctuations of the pressure signal remain low compared to the levels found under self-sustained oscillations and only reach up to 150 Pa in Fig. 7.

Flapping unsteadiness

Using the baseline injector geometry, one finds that certain operating conditions lead to unsteady dynamics. For intermediate power flames (up to 2.3 kW and $\phi = 0.50$), the flame is flapping between two configurations. Instantaneous images show that roughly 20% of the samples correspond to a V flame, whereas the flame remains attached 80% of the time with a conical shape. Using the same method as in Fig. 7 to display the contours of the instantaneous images one obtains Fig. 8 which features the two flame patterns. Samples were sorted out by identifying the two flame types to highlight the spontaneous flapping between the two flame shapes.

The pressure signals plotted in the right-hand side of Fig. 8 are recorded directly above the chamber, and corrected temporally to correspond to backplane microphone signals. They feature bursts with a variable time period of the order of 100 ms. The flapping unsteadiness described previously is accompanied by a high level of pressure fluctuations. Each burst features periodic oscillations in Fig. 8. with a peak frequency of 860 Hz, corresponding to a thermo-acoustic coupling. One may be led to think that the V and

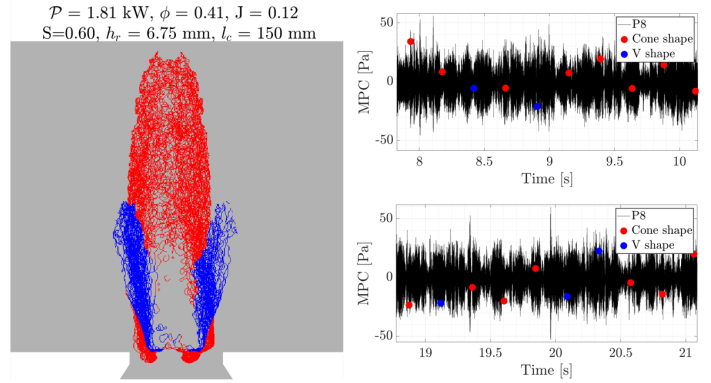


FIGURE 8: Bistable flame observed with the baseline geometry ($S = 0.60$, $h_r = 6.75 \text{ mm}$ and $l_c = 150 \text{ mm}$) at $\mathcal{P}_{th} = 1.81 \text{ kW}$ and $\phi = 0.41$. Left: contours of 100 line of sight OH^* intensity images, lying within the domain where chemical conversion takes place. The red and blue lines respectively correspond to conical and slightly lifted flame shapes. Right: Time evolution of pressure above the chamber. The red and blue dots in the time recordings mark the pressure levels corresponding to each of the flame shapes.

conical flame shapes correspond to specific phases in the thermo-acoustic cycle. This is not the case since the image recording is triggered at a rate that is not commensurate with the pressure signal frequency. It is also found, as shown on the right-hand side of Fig. 8, that the two patterns are not correlated with pressure bursts, a point that will be clarified in the future.

Other types of self-sustained oscillations (SSO) arise when the injector unit is equipped with the swirler 707 (swirl number $S = 0.60$). Oscillations occur when the system operates in an intermediate range of thermal power ($\mathcal{P}_{th} \in [1.5; 2.8] \text{ kW}$) and for global equivalence ratios between 0.35 and 0.50. This is the domain where one finds attached V-flames and lifted long flames. The pressure signal recorded in the plenum with MP2 features a frequency peak at 850 Hz for $l_c = 150 \text{ mm}$. Triggering the camera with this pressure signal and sweeping the gate delay based on this frequency yields the phase-averaged images displayed in Fig. 9 for one period of oscillation. The oscillation is characterized by a cyclic attachment (between phases $\pi/2$ and $5\pi/3$ in the cycle) and detachment of the flame from the injector. This mechanism is typically found in the operating domain where these SSO occurs. When the flame attaches to the injector, the maximum of OH^* intensity moves downwards to the injector outlet lips, where it remains until the flame detaches. The external shape of the flame front features a perturbation which forms a toroidal pattern convected upwards, entraining combustible reactants from the injector outlet [23].

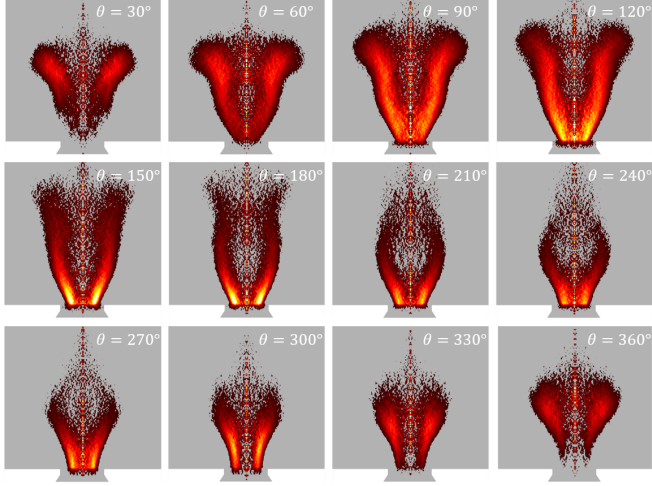


FIGURE 9: Phase averaged OH^* chemiluminescence images of the unstable flame at $\mathcal{P}_{th} = 2.31$ kW and $\phi = 0.42$ (Point 3), obtained with the baseline geometry: $S = 0.60$, $h_r = 6.75$ mm and $l_c = 150$ mm. The phase angle is denoted by θ .

This cyclic detachment and reattachment of the flame is observed for all the unstable operating points of the baseline injector geometry. It is also found in the other geometrical configurations, corresponding to a change in recess h_r . Effects of h_r and of chamber length l_c are discussed in section 5.

5 INFLUENCE OF RECESS AND CHAMBER LENGTH

It is well known from many previous experiments and theoretical studies that the chamber length notably influences the combustion stability. Effects of injection head location inside the injector defined by the recess h_r is less well documented but recent work on swirl spray flames indicate that this parameter is also influential [17]. The chamber length determines the frequency of the resonant modes which may potentially couple the acoustics of the system with the combustion dynamics. The recess length introduces a time delay between mixing and chemical conversion regions, and thus between flow variations and heat release rate fluctuations. The existence of a delay may lead to a growth of instability if the acoustic losses are low enough.

Effect of the recess length

The stable attached conical flame obtained with a large recess $h_r = 9.75$ mm at $\mathcal{P}_{th} = 1.62$ kW and $\phi = 0.42$ (point 2 in Fig. 6) becomes dynamically unstable when the injection head is moved upwards and the recess length is reduced to $h_r = 6.75$ mm. The attached flame blows out and reignites spontaneously. The power spectrum of the pressure signal (in red in Fig. 10) recorded at the chamber backplane features a bump with two broad peaks around

680 and 800 Hz that are not far from the eigenfrequency of the quarter wave eigenmode of the chamber. The peaks are less than 20 dB higher than the rest of the spectrum and the system is in this case weakly unstable. When the injector head recess is diminished to $h_r = 2.75$ mm the power spectrum features a well defined peak at 848 Hz (in blue in Fig. 10), that is more than 40 dB above the surrounding level, a clear indication of thermoacoustic coupling. Phase-averaged images of this instability exhibit a tulip shape as in Fig. 9 but with a larger toroidal structure detaching from the injector outlet lip. The chamber length slightly differs in this case from the baseline geometry used in Fig. 6 because a bottom metal piece is used to support the microphone. For this new length, the peak frequency corresponds to a quarter-wave axial mode with an open-end correction [24]:

$$f = \frac{c}{4(l_c + 0.4d_c)} \quad (5)$$

where c designates a mean speed of sound in the chamber. This speed depends on the gas temperature in the chamber which is not known, but it is possible to estimate this velocity from the frequency corresponding to the peak. In doing so one does not account for the fact that the instability frequency can be shifted with respect to the acoustic eigenfrequency by a certain amount. This shift of a few percent is here neglected. Using the chamber length and including the end correction, one obtains $c \simeq 653$ m s⁻¹ an estimate that will be used later on. The average temperature in the tube is thus about 1032 K, a few hundred degrees below the adiabatic flame temperature. One also notes the presence of a first harmonic at a frequency $f = 1696$ Hz at 30 dB below the fundamental and a second harmonic at a frequency $f = 2544$ Hz about 20 dB below the fundamental, indicating that the pressure response is slightly nonlinear. The third peak is higher than the second probably because it is close to the 3/4 wave eigenmode of the chamber and therefore encompasses non-linearity and linear excitation of the 3/4 wave mode.

Effect of the chamber length

The effect of the chamber length is now investigated by operating under the conditions corresponding to Fig. 9, $\mathcal{P}_{th} = 2.31$ kW and $\phi = 0.42$. The recess value is kept constant and equal to $h_r = 6.75$ mm. The system is now tested for three different chamber lengths $l_c = 115, 165$ and 265 mm (Fig. 11). Using a chamber length $l_c = 165$ mm one obtains a strong frequency peak at 847 Hz which is quite close to the peak observed for the same chamber length in Fig. 10. This peak also corresponds to a quarter-wave longitudinal chamber mode.

When the chamber length is diminished to 115 mm (the blue curve in Fig. 11), the spectrum features no peak and the flame is stable, lifted, and close to the outlet lips. When the chamber length is augmented to 265 mm (yellow curve), although there is a broad peak at a frequency close to 500 Hz which is close to the quarter-wave mode for that chamber length, the power spectrum

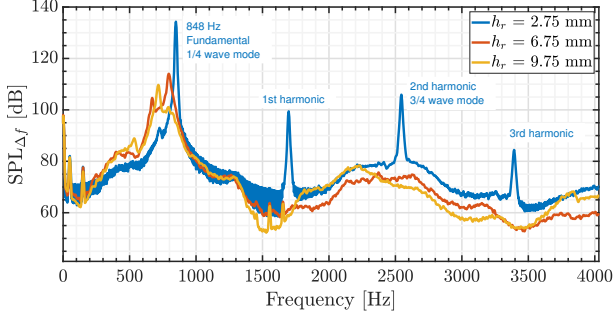


FIGURE 10: Spectral distribution of Sound Pressure Level obtained with constant chamber length $l_c = 165$ mm and $S = 0.60$ for the unstable operating point 2 presented in Fig. 6: thermal power $\mathcal{P}_{th} = 1.62$ kW and global equivalence ratio $\phi = 0.42$. Three values for the recess length h_r are presented: 2.75 mm, 6.75 mm and 9.75 mm.

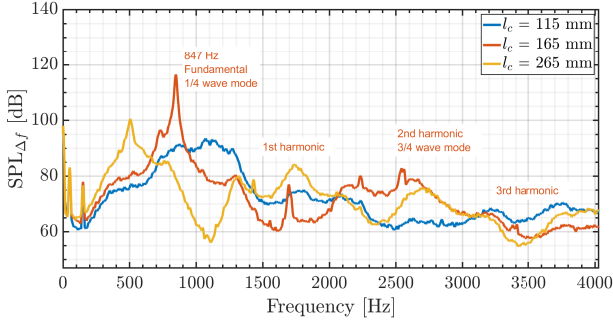


FIGURE 11: Spectral distribution of Sound Pressure Level obtained with constant recess length $h_r = 6.75$ mm and $S = 0.60$ for the unstable operating point 3 presented in Fig. 9: thermal power $\mathcal{P}_{th} = 2.31$ kW and global equivalence ratio $\phi = 0.42$. Three values for the quartz tube length l_c are presented: 115 mm, 165 mm and 265 mm.

is 20 dB below that found for $l_c = 165$ mm. For this operating point and a fixed injection head recess, changing the chamber length away from 165 mm allows suppressing the thermoacoustic instability. These observations confirm that self-sustained oscillations may be avoided by detuning the system by shifting the modal eigenfrequency to a higher or lower frequency range.

Comparison with a semi-analytical model

At this stage one may try to see if the instabilities observed experimentally can be interpreted by making use of an analytical framework relying on time lag concepts. It will also be shown that this model can be linked to a linear stability analysis which defines a necessary condition for instability in terms

of the phase of the flame transfer function. One wishes in particular to see if the changes in the recess length can be seen as a way to modify the delay between the injection and chemical conversion regions. Following the same reasoning as in [15] a one-dimensional model is used to estimate the delay between the injection point and the flame. One may then determine the product τf of the lag τ by the eigenfrequency of the acoustic mode f and see if this product belongs to the band of instability defined by [25]. According to this reference, a necessary condition for instability is that the product τf belong to a band centered around $1/2$. In principle, this unstable range corresponds to a τf interval $[1/4, 3/4]$. However, it is found in [15], that this band needs to be shifted with respect to the standard values and that it covers the interval $[0.45, 0.70]$. We will see later that the shift in the band location accounts for the impedance between the velocity disturbances acting on the flame and the pressure fluctuation, an impedance designated by $\zeta = p'/[\rho c v']$. This shift is explained in detail in [26]. In what follows we will use a band $[0.47, 0.80]$ that slightly differs from that considered in [15]. Following [25], the delay τ is the sum of the travel time between the injection ports and the injector outlet and the one corresponding to the distance from the outlet to the flame barycenter. The total delay is thus defined by convection inside and outside the injection unit:

$$\tau = \frac{h_r + h_i}{U_{inj}} + \frac{l_f}{U_b} \quad (6)$$

where h_r is the recess between the injection head and the injector outlet, h_i the vertical distance between the hydrogen injection holes and the top of the injection head, l_f designates the flame standoff distance and U_{inj} and U_b respectively designate the velocity inside the injector and the bulk velocity at the outlet.

As a first approximation, one may assume that $U_{inj} \simeq U_b$ and determine U_b from the volume flow rates of air and hydrogen: $U_b = 4(q_a + q_{H_2})/\pi d_c^2$. The length l_f is taken equal to HG determined from the time-averaged flame images since a spatial integration of the time lag is equivalent to the time lag computed from the outlet to the flame barycenter, by assuming that the velocity is constant. Finally, the frequency f is estimated as the quarter-wave longitudinal mode eigenfrequency, using Eq. 5. The value of τf is plotted for all the tested operating points and geometrical configurations in Fig. 12 where the unstable band is also shown. For different l_c , d_c , h_r , and two different swirlers, the unstable points fall inside the band. The previous model only provides a necessary condition for instability and indeed the unstable cases are inside the band shown in Fig. 12. There are however cases where τf falls in the band but where the system is operating in a stable fashion. To understand why this is so, one may consider the growth rate of small perturbations derived in linear stability analysis (see for example [26, 27]). For a system characterized by a flame transfer function \mathcal{F} defined as the ratio of relative heat release rate fluctuations to the relative velocity fluctuations $\mathcal{F} = [\dot{Q}'/\bar{Q}]/[v'/\bar{v}]$ and in which

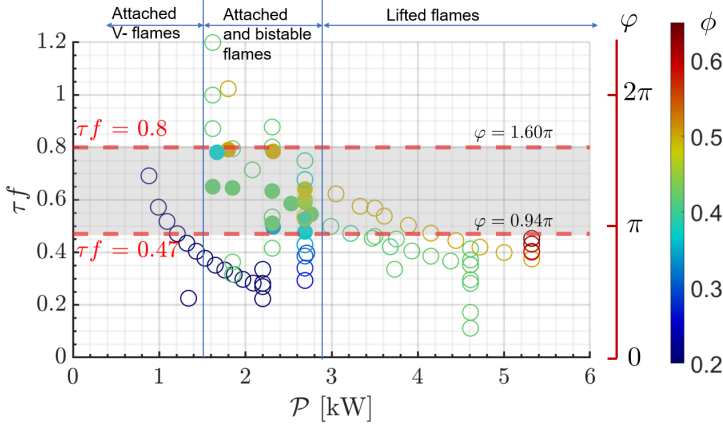


FIGURE 12: Values of the time delay between the CFI-X and the flame barycenter for all the operating points used with all geometrical configurations. The filled circles are unstable flames, while unfilled circles are used for stable flames.

the velocity disturbances acting on the flame are linked to the pressure by a specific impedance $\zeta = p'/[\rho c v']$ one finds that pressure perturbation growth is of the form $\exp(\omega_{1i}t)$ where the growth rate $\omega_{1i} \propto |\mathcal{F}|/|\zeta| \cos(\varphi_F - \varphi_\zeta)$ where φ_F and φ_ζ are the phases of the flame transfer function and impedance respectively [27]. Here, φ_F is approximated by $\omega\tau = 2\pi f\tau$. Perturbations will grow if $\cos(\varphi_F - \varphi_\zeta)$ is positive. In addition, the absolute value of ω_{1i} needs to be greater than the damping rate α characterizing the system. For this to be the case, the term $\cos(\varphi_F - \varphi_\zeta)$ should be sufficiently large, and this may require that this term be greater than 1/2. In addition $|\mathcal{F}|/|\zeta|$ should be sufficiently large. The first of these conditions will be satisfied if $-\pi/3 + \varphi_\zeta < \varphi_F < \pi/3 + \varphi_\zeta$. This defines a band extending over $2\pi/3$ and centered on φ_ζ . This band coincides with that introduced previously for a value of $\varphi_\zeta = 1.27\pi$ as can be seen in Fig. 12. This value for the impedance phase is in the range $[\pi, 3\pi/2]$ that is typically found for a system with a rigid backplane and a relatively small injector outlet [26]. This explains why the band is shifted with respect to the location initially presumed to be defined by $[\pi/2, 3\pi/2]$ centered on $\varphi_\zeta = \pi$ (corresponding to $1/4 < \tau f < 3/4$). Now, the second instability condition requires that the gain of the flame transfer function $G_F = |\mathcal{F}|$ be sufficiently large so that the growth rate exceeds the damping rate i.e so that $\omega_{1i} > \alpha$. This is probably not the case for the flame configurations obtained at the larger thermal powers which are lifted and less sensitive to incoming disturbances.

6 CONCLUSION

Systematic experiments are carried out with a swirling injection unit in which hydrogen is injected in cross-flow with the aim of promoting mixing and producing flames anchored at a dis-

tance from the injector outlet. Among the different types of stable flames it is found that detached flames are obtained when the thermal power exceeds a certain threshold.

The dynamical behavior of the various flames is investigated by varying the chamber length, the injection recess and the swirl number. Dynamical regimes leading to combustion instabilities are observed when the system operates in an intermediate range of thermal powers in particular when the flame is attached or in a bistable situation where it switches between attached and detached patterns, or when its geometry alternates from a V-shape to a conical shape. One special attached flame, formed with the highest swirl number injector, has the interesting property of remaining stable independently from the chamber length.

Self-sustained instabilities are characterized by a cyclic attachment-detachment of the flame and a periodic displacement of the maximum OH^* intensity indicating that the heat release rate in the flame is oscillating periodically. It is shown that these instabilities can be suppressed by varying the chamber length and the injection recess with respect to the outlet. The first parameter defines the resonant frequency f of the system while the second modifies the time delay τ between injection and flame.

A semi-analytical model, following previous work on gas turbine combustion instabilities, is then employed to derive a necessary condition for instability in which the product of the frequency by the delay $f\tau$ has to be in a certain band. The location of this band is shown to be related to the specific impedance linking the velocity disturbances acting on the flame to the pressure near the chamber backplane. It is found that the criterion expressed in terms of the $f\tau$ product can be translated in terms of the phase of the flame transfer function.

Using algebraic expressions to estimate the delay and the oscillation frequency it is found that all unstable operating points lie within this band. It is observed that the detached flames formed at higher thermal power levels may also have a product $f\tau$ that falls within the band but nevertheless do not lead to instability indicating that their structure is less sensitive to disturbances.

The injection scheme investigated in this article establishes under certain conditions flames that are detached from the solid boundaries and offer a reduced sensitivity to instability compared to attached flames. These flames are the most interesting because they reduce the thermal load on the injection unit and allow further mixing between hydrogen and air. These laboratory scale experiments are admittedly carried out in a situation that is not fully representative of engine conditions, in terms of air flow temperature and chamber pressure but the findings nevertheless provide insights on a scheme that combines crossflow injection and swirl and on the combustion dynamics of this system. However, the homogeneity of the mixture needs to be evaluated to assure that NOx emissions are close to those of a lean premixed flame. These issues are currently being addressed.

ACKNOWLEDGMENT

This work was partially supported by the FlyHy project of the Agence Nationale de la Recherche (ANR-21-CE05-0008).

REFERENCES

- [1] Khandelwal, B., Karakurt, A., Sekaran, P. R., Sethi, V., and Singh, R., 2013. “Hydrogen powered aircraft : The future of air transport”. *Prog. Aerosp. Sci.*, **60**, pp. 45–59.
- [2] Palies, P., 2022. “Challenges and Outlook for Hydrogen-Based Aviation”. *AIAA Paper 2022-3378*, p. 15.
- [3] Zeldovich, Y., 1946. “The oxidation of nitrogen in combustion and explosions”. *Acta Physicochem USSR*, p. 577.
- [4] Reichel, T. G., Terhaar, S., and Paschereit, O., 2015. “Increasing Flashback Resistance in Lean Premixed Swirl-Stabilized Hydrogen Combustion by Axial Air Injection”. *J. Eng. Gas Turbines Power*, **137**(7), p. 071503.
- [5] Sattelmayer, T., Mayer, C., and Sangl, J., 2016. “Interaction of Flame Flashback Mechanisms in Premixed Hydrogen–Air Swirl Flames”. *J. Eng. Gas Turbines Power*, **138**(1), p. 011503.
- [6] Reichel, T. G., Terhaar, S., and Paschereit, C. O., 2018. “Flashback Resistance and Fuel–Air Mixing in Lean Premixed Hydrogen Combustion”. *J. Propul. Power*, **34**(3), pp. 690–701.
- [7] Baumgartner, G., and Sattelmayer, T., 2013. “Experimental Investigation of the Flashback Limits and Flame Propagation Mechanisms for Premixed Hydrogen–Air Flames in Non-Swirling and Swirling Flow”. In ASME, Paper No: GT2013-94258, V01AT04A010.
- [8] Leroy, M., Mirat, C., Renaud, A., and Vicquelin, R., 2022. “Stabilization of Low-NOx Hydrogen Flames on a Dual-Swirl Coaxial Injector”. *J. Eng. Gas Turbines Power*, **145**(2), p. 021021.
- [9] Marragou, S., Magnes, H., Poinso, T., Selle, L., and Schuller, T., 2022. “Stabilization regimes and pollutant emissions from a dual fuel CH₄/H₂ and dual swirl low NOx burner”. *Int. J. Hydrogen Energy*, **47**(44), p. 19275.
- [10] Aguilar, J. G., Æsøy, E., and Dawson, J. R., 2022. “The influence of hydrogen on the stability of a perfectly premixed combustor”. *Combust. Flame*, **245**(112323).
- [11] Sullivan-Lewis, E., and McDonell, V., 2016. “Predicting Flameholding for Hydrogen and Natural Gas Flames at Gas Turbine Premixer Conditions”. *J. Eng. Gas Turbines Power*, **138**(12), p. 121502.
- [12] Karyeyen, S., Feser, J. S., and Gupta, A. K., 2019. “Hydrogen concentration effects on swirl-stabilized oxy-colorless distributed combustion”. *Fuel*, **253**, pp. 772–780.
- [13] Dahl, G., and Suttrop, F., 1998. “Engine control and low-NOx combustion for hydrogen fuelled aircraft gas turbines”. *Int. J. Hydrogen Energy*, **23**(8), pp. 695–704.
- [14] Juniper, M. P., and Candel, S. M., 2003. “The stability of ducted compound flows and consequences for the geometry of coaxial injectors”. *J. Fluid Mech.*, **482**, pp. 257–269.
- [15] Straub, D. L., and Richards, G. A., 1998. “Effect of Fuel Nozzle Configuration on Premix Combustion Dynamics”. In ASME, Paper No: 98-GT-492, V003T06A044.
- [16] Æsøy, E., Indlekofer, T., Gant, F., Cuquel, A., Bothien, M. R., and Dawson, J. R., 2022. “The effect of hydrogen enrichment, flame-flame interaction, confinement, and asymmetry on the acoustic response of a model can combustor”. *Combust. Flame*, **242**(112176).
- [17] Rajendram Soundararajan, P., Durox, D., Renaud, A., and Candel, S., 2022. “Impact of spray dynamics on combustion instabilities investigated by changing the atomizer recess in a swirl combustor”. *Combust. Flame*.
- [18] Prieur, K., Durox, D., Vignat, G., Schuller, T., and Candel, S., 2017. “Experimental determinations of Flame Describing Functions of swirling spray flames”. In Colloque INCA, Châteaufort, France.
- [19] Kolla, H., Grout, R. W., Gruber, A., and Chen, J. H., 2012. “Mechanisms of flame stabilization and blowout in a reacting turbulent hydrogen jet in cross-flow”. *Combust. Flame*, **159**(8), pp. 2755–2766.
- [20] Vignat, G., Durox, D., and Candel, S., 2022. “The suitability of different swirl number definitions for describing swirl flows: Accurate, common and (over-) simplified formulations”. *Prog. Energy Combust. Sci.*, **89**(100969).
- [21] Vignat, G., Durox, D., Prieur, K., and Candel, S., 2019. “An experimental study into the effect of injector pressure loss on self-sustained combustion instabilities in a swirled spray burner”. *Proc. Combust. Inst.*, **37**(4), pp. 5205–5213.
- [22] Fiala, T., Sattelmayer, T., Gröning, S., Hardi, J., Stützer, R., Webster, S., and Oswald, M., 2017. “Comparison Between Excited Hydroxyl Radical and Blue Radiation from Hydrogen Rocket Combustion”. *J. Propul. Power*, **33**(2), pp. 490–500.
- [23] Durox, D., Schuller, T., and Candel, S., 2005. “Combustion dynamics of inverted conical flames”. *Proc. Combust. Inst.*, **30**(2), pp. 1717–1724.
- [24] Rayleigh, J. W. S., 1896. *The Theory of Sound*, first ed., Vol. 2, p.197, Appendix A. Cambridge University Press.
- [25] Richards, G. A., and Janus, M. C., 1998. “Characterization of Oscillations During Premix Gas Turbine Combustion”. *J. Eng. Gas Turbines Power*, **120**(2), pp. 294–302.
- [26] Rajendram Soundararajan, P., Durox, D., Renaud, A., Vignat, G., and Candel, S., 2022. “Swirler effects on combustion instabilities analyzed with measured FDFs, injector impedances and damping rates”. *Combust. Flame*, **238**, p. 111947.
- [27] Schuller, T., Poinso, T., and Candel, S., 2020. “Dynamics and control of premixed combustion systems based on flame transfer and describing functions”. *J. Fluid Mech.*, **894**, p. P1.